Cascaded nonlinearity induced spatial domain effects in a high power femtosecond optical parametric oscillator

I. STASEVIČIUS[1,2,*] AND M. VENGRIS[1,2]

[1]*Vilnius University Laser Research Center, Saulėtekio av. 10, LT-10223 Vilnius, Lithuania*
[2]*Light Conversion, Keramikų 2b, Vilnius, LT-10223, Lithuania*
[*]ignas.stasevicius@lightcon.com

Abstract: We have investigated the effect of cascaded optical nonlinearity on the spatial beam properties of a femtosecond optical parametric oscillator (OPO). The OPO was operated with a tunable phase mismatch by varying the angle of the nonlinear crystal. The cascaded nonlinearity induced self-focusing and defocusing changed resonator's stability and impacted mode properties. With tuning of a phase mismatch, the calculated parabolic part of cascaded nonlinearity lens focal length changes from $f \sim 30$ mm ($D \sim 33$ m^{-1} at $\Delta\theta \sim -0.5^o$) to infinity and back to $f \sim -110$ mm ($D \sim -9$ m^{-1} at $\Delta\theta \sim 0.9^o$) in the LBO nonlinear crystal. Such high power nonlinear lenses in a cavity operated near its stability limit promoted the generation of axially asymmetric or pass-to-pass unstable resonator modes. It was shown that phase mismatched optical parametric oscillation changes the physical character of the resonator from linear to ring-like with two nonlinear crystals having two different focusing powers. Calculations showed that the QCN induced spatial nonlinear phase should lead to severe longitudinal chromatic aberrations for broad spectrum pulses. A numerical simulation in XYZ spatial domain and calculations using ABCD matrix approach confirmed the physical mechanisms underlying the experimental results and allowed for the interpretation of the observed effects.

1. Introduction

High intracavity intensities in femtosecond synchronously pumped optical parametric oscillators induce temporal and spatial nonlinear effects in the crystals used for amplification. As OPOs are scaled to higher power, the nonlinear lensing can distort the resonant spatial modes of the cavity. These effects must be properly understood in order to design the OPOs that achieve performance comparable to theory. Output power scaling is required by the laser machining, high harmonic generation, nonlinear imaging and other applications. In particular in the nonlinear microscopy, the main push towards higher powers is an increase of the scanning speeds and additional power losses in the microscope system induced by pulse pickers, spatial light modulators and other components. The observed nonlinear temporal domain effects are well explored and include temporal soliton formation [1,2], temporal simulton formation [3], four-wave mixing [4,5], cascaded quadratic nonlinearities (QCN) [6,7] and other effects. The nonlinear spatial domain effects such as self-focusing and defocusing remain largely unexplored in optical parametric oscillators, but are well analyzed in a number of other single pass and laser resonator applications. Spatial domain modelling of optical parametric amplifiers shows that the nonlinear spatial domain effects are too weak to have an impact to a single pass OPA system if the peak power is lower than the critical power. If the peak power is larger than the critical power, self-refraction distorts beam quality [8,9]. Intracavity self-focusing is well analyzed and is a mechanism underlying the ubiquitous Kerr lens mode locking in laser oscillators. The resonator stability is sensitive to minute changes of the self-focusing lens, so spatial effects are important even at powers well below critical [10,11]. The self-focusing and defocusing are observed in a single pass

quadratic medium pulse compressors, where cascaded effect leads to high values of effective nonlinearity [12,13,14]. In addition to that, the classical Z-scan setup was used to directly observe QCN induced spatial domain effects [15,16]. The evidence of the QCN impact to pulse characteristics was also observed in the femtosecond optical parametric oscillators [15,16,17], but an investigation of QCN induced self-focusing and defocusing impact to spatial mode is still lacking.

The QCN is a nonlinear process, whereby a wave experiences a nonlinear conversion to a different frequency (travelling at different phase velocity) and a subsequent back-conversion to the original frequency. As a net result, the frequency of the wave remains unchanged, but the wave experiences an effective phase shift (delay), compared to purely linear propagation. This process is equivalent to the propagation in the medium with nonlinear refractive index proportional to $d_{eff}^2/\Delta k$, hence allowing to control the sign of the nonlinearity by changing the detuning Δk [18]. The effect manifests both in time and in spatial domain as a phase modulation term. It is also important to note that the nonlinear QCN-induced phase shifts experienced by pulses or beams in difference frequency generation (DFG) and second harmonic generation (SHG) have opposite signs [16,19]. For our experimental conditions (the DFG OPO based on LBO) the negative crystal detuning induces positive (focusing) QCN and the positive crystal detuning induces negative (defocusing) QCN.

In this paper, we demonstrate that QCN induces effective focusing / defocusing nonlinear lenses reaching focal lengths of $f \sim 30$ mm ($D \sim 33$ m^{-1}) / $f \sim -110$ mm ($D \sim -9$ m^{-1}). Such large lens powers inevitably change the stability of resonator. Both operation near the stability range and resonator astigmatism lead to the deterioration of spatial beam properties. Generation of axially asymmetric or pass-to-pass unstable resonator modes were observed. It was shown that operating the crystal with phase mismatch changes the physical operation of resonator from linear to ring-like with two nonlinear crystals having two different focusing powers. These findings lead to a better understanding of how to design a high power femtosecond optical parametric oscillator with optimal beam characteristics.

2. Experimental procedures

The optical setup used for the experiments is shown in Fig. 1. The optical parametric oscillator is pumped by the second harmonic of Yb:KGW based femtosecond oscillator (Flint, Light Conversion). Pump oscillator emits 12 W of average power with 140 fs pulse duration (Gaussian shape fit) at 1030 nm central wavelength and 76 MHz repetition rate. Pump light is frequency doubled in 2.5 mm length LBO crystal with AR coatings, where 6 W of average power at 515 nm is generated with 50% conversion efficiency, the pulse duration of the second harmonic is 135 fs (Gaussian shape fit). Fundamental light is filtered out, and pump light is delivered to pump the optical parametric oscillator. Pump light is focused to the spot size of 50 μm, which is the size of resonating signal mode's radius. When operating at maximum output power, the calculated signal intensity reaches 20 GW/cm^2 in LBO crystal. Cavity mirrors M6, M7, M8, M9 are highly reflective in the range from 770 nm to 970 nm. The used mirror design is a simple λ/4 stack with a low group velocity dispersion throughout the wavelength range (decreasing from +20 fs^2 at 770 nm to −20 fs^2 at 970 nm). As this study was aimed to the spatial domain properties of the generated beam, the time domain measurements of the generated pulses and wavelength tunability of a similar experimental setup are discussed in our previous papers [20,21]. For this study a fixed wavelength of 860 nm at the center of the mirrors' reflection curve was used which corresponds to an idler wavelength of 1280 nm. The used concave mirrors (R= −200 mm) focus the resonating beam into the nonlinear crystal. The angle of incidence to spherical mirrors is 3°. This angle determines the astigmatism of the resonator. We will adopt the term 'tangential plane' or 'X plane' further in the paper to denote the plane in which this angle is formed. One of the curved mirrors, M5, is highly reflective in 770 to 970 nm range and has high transmittance at the

pump wavelength of 515 nm. The output coupler OC with 10% of transmission in the wavelength range from 770 to 970 nm was used. Nonlinear 2.5 mm long LBO crystal (crystal $\theta = 14°$, type I, Eksma Optics) was used as OPO gain material. The crystal was AR coated at 1030 nm + 515 nm. The crystal reflection coefficient at the signal wavelength of 860 nm was experimentally measured to be 4%, therefore optimized coatings would lead to even higher output powers, but it does not impede the spatial domain investigation. The crystal was mounted on a precision rotation stage allowing the control of phase matching angle, which was later recalculated to internal angle. The pump beam is polarized in sagittal plane (Y) and the crystal is rotated in this plane for angular phase matching. Since the rotation of the LBO crystal slightly misaligned the resonator cavity, the end mirror M8 was adjusted to realign the resonator to the maximum output power after each angle change. The two curved mirrors M5 and M6 are put on the translation tables to allow changing the stability of the resonator. Beam dump discarded the remaining pump and idler beams. Fused silica windows GP1 and GP2 (14 mm thickness, AR coated for 650-1000 nm, R <0.5%) were inserted into the cavity to ensure positive group delay dispersion. The total calculated group delay dispersion of the cavity was ~1900 fs^2 at 860 nm. OPO cavity length was adjusted by moving the output coupler placed on a translation stage, to enable finding synchronous pumping conditions. The movement of translation table is also used to stabilize the central wavelength of OPO generation. Ambient temperature deviations alter the lengths of the cavities of the pump laser and the OPO. For a femtosecond OPO to generate, the synchronous pumping condition has to be always satisfied. Under small temperature changes, the generation shifts to signal wavelengths with larger or smaller group velocities, determined by the cavity GDD. Larger values of intracavity GDD imply that the differences of group velocities between neighboring wavelengths are larger, which makes central wavelength of the OPO less sensitive to the ambient temperature changes. In this study, we aimed to investigate the spatial effects in the OPO rather than produce the shortest possible output pulses, therefore we opted for operation with large GDD of the OPO cavity. Positive GDD values are easier to realize experimentally, by inserting additional material in the cavity. Note that synchronously pumped OPOs are unique in their ability to operate under phase mismatch. In quasi continuous wave optical parametric oscillators, a change of the crystal angle would shift the central wavelength to the phase matched one and no DFG induced QCN effects could be observed.
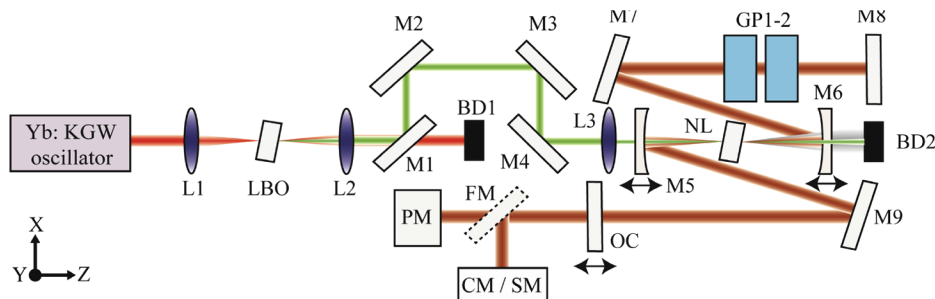
Fig. 1. Experimental setup. L1, L2, L3 – lenses for second harmonic generation, collimation and pump light focusing respectively. M1, M2, M3, M4 mirrors for pump light delivery with high transmission at fundamental wavelength. M5, M6 – curved resonator mirrors on a translation table. M7, M8, M9 – plane resonator mirrors. OC – output coupler, NL – nonlinear crystal. BD1, BD2- beam dump. FM – flip mirror, PM – power meter, CM - camera, SM – spectrometer. GP1-2 intracavity Fused Silica glass plates.

Average power of output radiation was measured using a power meter (Nova-2, Ophir) equipped with a thermopile detector (30(150)A-BB-18, Ophir). Radiation spectra were recorded using a spectrometer (STS-NIR, Ocean Optics), pulse durations were measured using a scanning

autocorrelator (Geco, Light Conversion), and the beam profile was measured with FLIR Chameleon camera (CMLN-13S2C-CS) at 30 cm distance from the output coupler.

3. Numerical modelling

The theoretical description of the optical parametric oscillator resonator modes requires detailed analysis of propagation equations of the beams in the nonlinear crystal and in a cavity. In this work, a system of coupled nonlinear equations is solved, given by Eq. (1) to (3)

$$\frac{\partial E_i}{\partial z} + \frac{i}{2\,k_i}\left(\frac{\partial^2 E_i}{\partial x^2} + \frac{\partial^2 E_i}{\partial y^2}\right) = -i\sigma_i E_s^* E_p e^{-i\Delta kz} - i\beta_i E_i(|E_i|^2 + \gamma_{is}|E_s|^2 + \gamma_{ip}|E_p|^2), \quad (1)$$

$$\frac{\partial E_s}{\partial z} + \frac{i}{2\,k_s}\left(\frac{\partial^2 E_s}{\partial x^2} + \frac{\partial^2 E_s}{\partial y^2}\right) = -i\sigma_s E_i^* E_p e^{-i\Delta kz} - i\beta_s E_s(|E_s|^2 + \gamma_{is}|E_i|^2 + \gamma_{sp}|E_p|^2), \quad (2)$$

$$\frac{\partial E_p}{\partial z} + \rho_p\frac{\partial E_p}{\partial y} + \frac{i}{2\,k_p}\left(\frac{\partial^2 E_p}{\partial x^2} + \frac{\partial^2 E_p}{\partial y^2}\right) = -i\sigma_p E_i E_s e^{i\Delta kz} - i\beta_p E_p(|E_p|^2 + \gamma_{ip}|E_i|^2 + \gamma_{sp}|E_s|^2). \quad (3)$$

Electric fields E_i, E_p, E_s are the electric field amplitudes of idler (λ_i =1280 nm), signal (λ_i =860 nm), and pump (λ_i =515 nm), respectively. The electric field was assumed to be CW in the time domain, the peak intensity of the pump was calculated as $1,62\,P_{ave}/f_{rep}\pi\,\omega_0^2\,\tau$ with an experimentally measured pump average power P_{ave} = 6 W, repetition rate f_{rep} = 76 MHz, beam radius ω_0 = 50 μm, pump pulse duration of τ = 135 fs. The spatial walk off of extraordinary pump beam is accounted for by walk-off angle ρ_p = 7.6 mRad. Beam propagation vectors are denoted $k_{i,s,p}$, $\sigma_{i,s,p}$ are nonlinear coupling coefficients defined as $2\,\pi\,d_{eff}/\lambda_{i,s,p}n_{i,s,p}$ with d_{eff} = 0.86 pm/V . $\beta_{i,s,p}$ is an electronic Kerr self-phase modulation coefficient defined as $n_2\,\varepsilon_0\,n_{i,s,p}\,\pi\,c/\lambda_{i,s,p}$ with $n_2 = 3\times10^{-20}$ m²/W. $\gamma_{is,ip,sp}$ is a cross-phase modulation coefficient, γ_{is} = 2 for parallel polarizations and $\gamma_{ip,sp}$ = 2 / 3 for orthogonal polarizations. Derivation and definition of the nonlinear coupling, self- and cross-phase modulation coefficients are given in [22,23]. Phase mismatch Δk is defined as $\Delta k = k_p - k_s - k_i$. After each pass through the crystal, the propagation in resonator is simulated. Free space propagation is solved in spatial frequency domain using free space transfer function, lens transfer function is applied in real space domain, non-zero angle of incidence of spherical mirrors leads to different focal lengths for horizontal and vertical planes as shown in [24]. During the returning pass, the signal propagates through the nonlinear crystal without pump and idler beams applied. The Eq. (2) is solved again with only self-phase modulation term. Resonator losses and output coupler transmission are applied. Afterwards, the signal beam is returned to the crystal for another cycle with a new pump beam and an idler beam starting from noise. This process is continued until the signal output power saturates, i.e. the resonator losses become equal to the gain. After multiple passes through the cavity, the spatial resonator mode settles with fixed pass to pass beam width and output power.

To save the computational cost, the coupled equations are solved in spatial domain only, with time domain effects, such as dispersion and finite pulse width, excluded. This induces calculation error, but the model is accurate enough for the calculation of the spatial domain mode parameters. The ratio between simulated and experimentally measured output powers provides approximate overestimation of the intracavity intensity, which in our case was around 25%. The temporal walk-off between the signal (860 nm) and the second harmonic pump (515 nm) pulse in the 2.5 mm LBO crystal is 110 fs. The pump pulse width was 135 fs, the generated signal had a pulse width of 180 fs. If the pulses coincide at the center of the crystal for the most optimal temporal overlap (signal delayed by half the walk-off value of 55 fs at the entrance of the crystal), the walk-off is 30 - 40% of the signal and pump pulse durations. Therefore, an overestimated simulated intensity should stem from the overestimated effective gain which should be decreased because of a temporal walk-off. This was not accounted for, because of the semi-empirical

origin of the effective gain damping term and acceptable correspondence between simulated and experimental results. Moreover, a quasi-CW model that uses the peak gain of the pulsed pump was shown to be quite accurate estimate of the simulated gain of the OPO [25].

In order to compare the experimental camera beam measurements to the simulated ones for the case of an unstable resonator, the last 20 passes of the simulated beam were averaged when steady output power state was reached. In the case of stable resonator, the mode radii remain the same pass to pass and no averaging was needed.

The nonlinear phase is induced by the nonlinear part of the system of Eqs. (1)–(3). During each step of the split step algorithm, this nonlinear part is solved and nonlinear phase shift is extracted independently from linear phase. The nonlinear phase dependence on the spatial coordinate results in a spatial nonlinear phase shift. Fitting this nonlinear phase shift with parabola allows approximating the effect of nonlinearity as a nonlinear lens which is accurate for the center of the beam. Both coordinates were fit independently and the extracted lens' values were later used for ABCD matrix resonator stability calculation. The relationship between the nonlinear phase $\Delta\varphi_{NL}$ and the effective nonlinearity n_2^{eff} is defined as $\Delta\varphi_{NL} = k_0 \, L \, n_2^{eff} I$, where k_0 is a wavevector, L is crystal length, and I is intensity.

The resonator stability was calculated using the ABCD matrix formalism. The stable resonator is obtained when the round-trip matrix terms are in the range of $-1 < (A + D)/2 < 1$. The $(A + D)/2$ parameter is calculated separately for each of the transverse coordinates. The four-mirror folded resonator consists of two stability zones with different mode sizes in the output coupler and in nonlinear crystal. Throughout the paper, we used terminology zone I and zone II, the transition of both zones happens when $(A + D)/2$ reaches -1. We have operated around this transition point in our experimental setup, as being close to the stability limit makes the resonator more sensitive to the nonlinear focusing / defocusing. Operation near the stability limit of $(A + D)/2 \sim 1$ makes the resonator just as sensitive to the focusing / defocusing and should produce similar results. On the other hand, experimentally probing both stability zones near this stability limit would be hard to perform, as both zones would be separated by whole stability zone width, as will be further shown in a linear stability map of Fig. 2(A).

One important observation is that while operating with phase mismatch the nonlinear lenses for forward and backward propagations are different. On a forward pass, nonlinear focusing / defocusing stems from the material plus cascaded nonlinearity and on a backward pass only the material nonlinearity contributes to the nonlinear focusing. This means that in effect the investigated resonator is not a linear one, but rather acts as a ring resonator with two nonlinear crystals having two different focusing powers, because the resonating beam experiences a different nonlinear lens during its return pass. To account for this, the resonator was analyzed as a ring resonator using ABCD formalism with resonator cavity ABCD matrix defined by a cavity round trip, as shown in [26]. A nonlinear lens was included as a simple lens matrix with a known focal length, calculated from the parabolic part of simulated nonlinear phase. A further stability analysis needs to be done while using the ABCD matrix of a self-focusing nonlinear medium as shown in [26], but our approach of using a simple lens matrix was sufficient to allow interpretations of the first experiments. It is interesting to note, that only with the account of nonlinear focal lengths the stability and mode sizes could be matched to the values observed experimentally. The $(A_Y + D_Y)/2$ parameter for a resonator without nonlinear focal lengths was ~ -0.85, while inserting the nonlinear focal lengths with zero phase mismatch ($f_{NL} \sim 55$ mm for zone II) shifted it close to the stability limit with a $(A_Y + D_Y)/2$ value of ~ -0.98. The calculated nonlinear focal length was dependent on the mode size as seen from Eq. (4). The mode sizes in a crystal were 62 μm (zone I) and 50 μm (zone II). A return pass nonlinear focal length with zero phase mismatch $\Delta\theta \sim 0^o$ was calculated to be 125 mm in zone I and 55 mm in zone II. A forward pass parabolic fit of the cascaded nonlinear phase depends on the crystal detuning. It was calculated to be: zone I focal lengths ranged from +125 mm ($\Delta\theta \sim -0.25^o$) to infinity
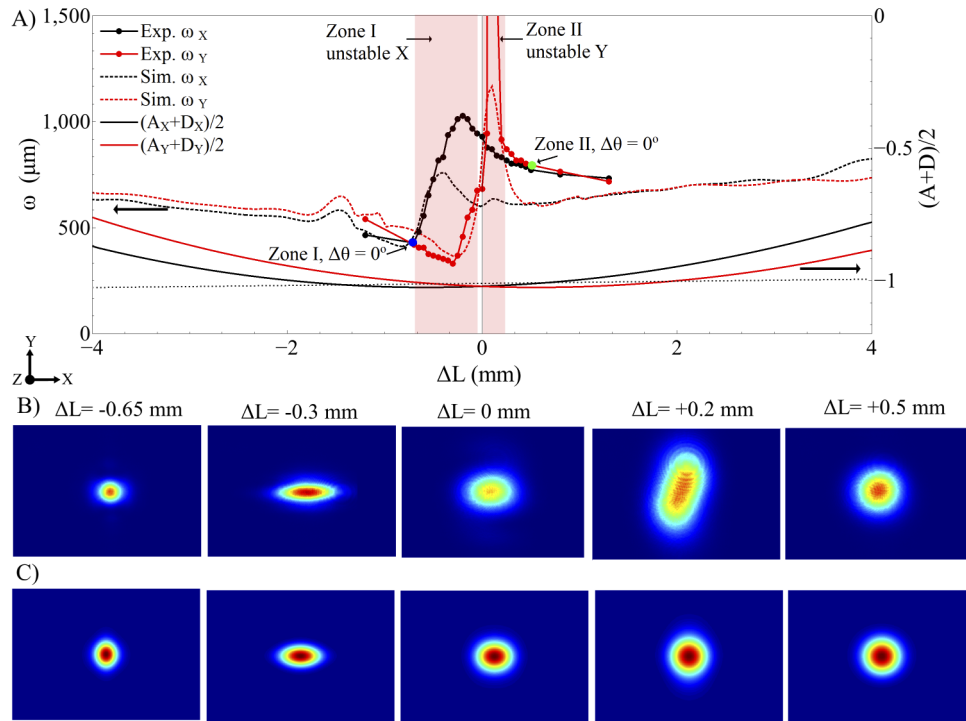
Fig. 2. A) The experimentally measured and numerically simulated second-moment radii (2σ) dependence on the distance between curved resonator mirrors and resonator stability parameter $(A + D)/2$. The radii and stability are calculated separately for tangential (X) and sagittal (Y) planes. Blue and green points indicate the distances ΔL where the resonator was aligned for the zone I and zone II cascaded nonlinearity experiments. B) Experimentally measured beam profiles corresponding to different values of ΔL. C) Numerically simulated output beam profiles corresponding to different values of ΔL. In all panels signal central wavelength is fixed at 860 nm and the crystal angle is fixed at $\Delta\theta=12.6°$.

$(\Delta\theta \sim 0.4^o)$ and back to -250 mm $(\Delta\theta \sim 0.65^o)$. Zone II focal lengths ranged from $+30$ mm $(\Delta\theta \sim -0.5^o)$ to infinity $(\Delta\theta \sim 0.25^o)$ and back to -110 mm $(\Delta\theta \sim 0.9^o)$. As the nonlinear lenses were inserted in an approximate geometrical focus of the linear resonator, the effect of the lenses was not as evident, but nevertheless experimentally observable. A major difference in forward and backward propagation nonlinear focal lengths clearly indicates that ring resonator with two different nonlinear crystals formalism is more suitable for a phase mismatched optical parametric oscillator description, even though experimentally it is assembled as a linear one.

The parabolic fit nonlinear lens focal length can also be calculated as [26]:

$$f_{NL} = \frac{\pi \, \omega^4}{8P \, n_2 L},$$

(4)

Where w is beam radius, P – peak power, n_2 – effective nonlinearity, L – propagation length in a crystal. Direct calculation of Eq. (4) while inserting zone radii 62 μm (zone I) and 50 μm (zone II), internal peak powers at the peak of the tuning curve ~ 630 kW and nonlinear refractive index of $n_2 \sim 3 \times 10^{-20}$ m²/W results in nonlinear focal lengths of $f_{NL} = 98$ mm (zone I) and $f_{NL} = 42$ mm (zone II), which are close to numerically simulated values for a returning pass with material's contribution only.

4.   Results and discussion

In order to analyze the nonlinear focal length's impact to resonator's mode formation, the stability of phase-matched operation was investigated. The signal wavelength was fixed at 860 nm and the OPO crystal angle was fixed at $\theta \sim 12.6^o$. The phase mismatch was minimized for maximum output power and low cascaded nonlinearity influence to the resonator stability. The distance between resonator's curved mirrors was changed (both of the mirrors were translated simultaneously by ΔL) and resonator output mode was measured with a camera. The results are shown in Fig. 2. Figure 2(A) shows the measured and numerically simulated second-moment radii (2σ) in both tangential (X) and sagittal planes (Y). Figure 2(B) shows measured and Fig. 2(C) shows numerically simulated beam profiles. The discrepancy between the measured and numerically simulated beam profiles (especially at the distance of ΔL= +0.2 mm) could be explained by an error of estimating the exact curved mirrors' angles of incidences. This could lead to more astigmatic cavity in the experiment which would lead to higher output beam ellipticity. As the mirrors are translated, the resonator stability approaches a stability limit at $(A + D)/2 = -1$. The non-zero angle of incidence of the resonator curved mirrors lead to different stability diagrams for both planes, shown in Fig. 2(A). As described in the section of numerical modelling, the material's contribution nonlinear focal lengths were included in ABCD matrix calculation and the $(A + D)/2$ parameter was calculated. The -1 value of the stability parameter is approached in different ΔL detuning values for both of the tangential (X) and sagittal (Y) planes. That leads to strong changes in the ellipticity of the beam as the distance ΔL and stability is changed. The red colored zones show the regions of experimentally observed highly elliptical X and Y beams, named correspondingly zone I and zone II.

It is interesting to note, that the insertion of the nonlinear lenses shifts the calculated stability below values of -1 to a range where resonator is unstable. The calculated mode sizes in a crystal are 62 µm (zone I) and 50 µm (zone II) and these lead to largely different nonlinear focal lengths because of the 4th power dependence as shown in Eq. (4). The calculated nonlinear focal lengths are much smaller in zone II (f_{NL} = 125 mm in zone I and 55 mm in zone II), so the stability is stronger shifted below -1 in zone II than zone I. This leads to a larger sagittal plane (Y) beam ellipticity in zone II.

In order to probe the influence of cascaded nonlinearity to the mode formation, the mirror distance was fixed at two stable resonator points: ΔL=- 0.8 mm (close to unstable zone I) and ΔL = 0.6 mm (close to unstable zone II). The points are indicated in Fig. 2(A) as blue and green dots. This allowed working with a stable resonator but being close enough to the edge of the stability zone to probe the nonlinear focusing / defocusing effects. As the nonlinear crystal was rotated, the resonator was realigned to maximum output power by the end mirror and resonator length was adjusted to resonate the wavelength of 860 nm. The measured output power dependence on crystal rotation angle is given in Fig. 3 for both zone I and zone II. The measured pulse duration at the peak of the tuning curve is 180 fs, the pulse is chirped with a pulse quality of $\Delta \nu \, \Delta \tau \sim 0.85$. The mode radius at the crystal is smaller in zone II, making the effect of pump beam walk-off more evident. The walk-off decreases the effective crystal length, which in turn increases the acceptance angle of the crystal. This leads to an increase in the width of the power tuning curve. On the other hand, shorter effective crystal length leads to the decrease of the output power as is evident from the figures. The positive angle offsets of zone II starting at $\Delta \theta \sim 0.5^o$ lead to an asymmetry of the otherwise symmetric tuning curve. Further investigation will reveal that this angle range leads to an unstable resonator. Surprisingly, the interaction of the unstable signal beam with the pump is sufficient enough to support the generation and even be at higher power levels than those resulting from the stable signal beam, at the same crystal detuning.

Since the largest effects of the cascaded quadratic nonlinearities on the output beam of the OPO occur around the edges of the resonator stability range, we investigated the beam properties as a function of angular detuning of the OPO crystal near the instability zones I and II.
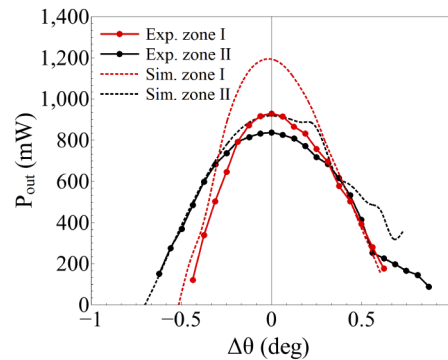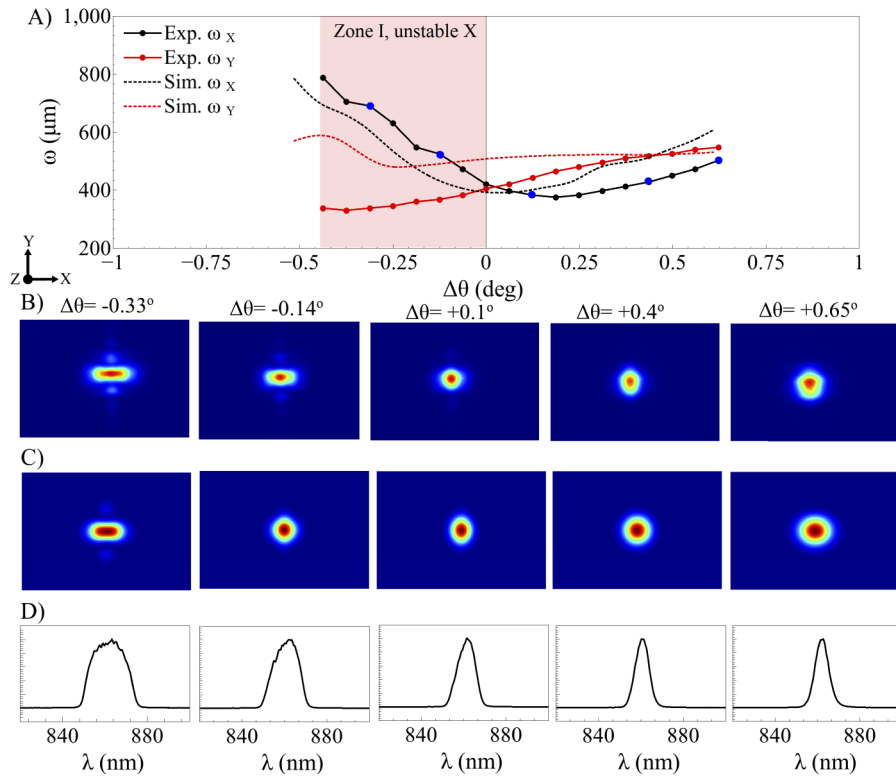
Fig. 3. The experimentally measured and numerically simulated output power dependence on the nonlinear crystal detuning when the resonator was aligned for the zone I and zone II cascaded nonlinearity experiments. Signal central wavelength is fixed at 860 nm.

Unstable zone I. First, the dependence of the output beam profiles on the phase matching angle was measured when the resonator was fixed at $\Delta L = -0.8$ mm curved mirror distance (close to unstable zone I). The resulting dependencies for sagittal and tangential beam radii are shown in Fig. 4(A). The blue points correspond to the measured beam profile (Fig. 4(B)), simulated beam profile (Fig. 4(C)) and measured spectra (Fig. 4(D)) at these exact angle offsets. The radii change indicate that the negative crystal offsets lead to positive (focusing) cascaded nonlinearity which shifts the stability towards configuration supporting highly elliptical mode in tangential (X) direction. The red area indicates the unstable angle offset region when resonator is "pushed" towards the unstable part of zone I shown in Fig. 2(A). The trends of change in the simulated beam profiles closely resemble the experimental ones, albeit the simulated second-moment radii show higher deviation from the experiment. The reason for the discrepancy may be related to the contribution of dot-like vertical mode structure at large negative crystal offsets. The measured spectra in Fig. 4(D) indicate the contribution of SPM to spectral broadening. As the crystal is offset to negative angles, positive cascaded nonlinearity adds up to the material nonlinearity and together with positive cavity group delay dispersion leads to the broadening of the output spectrum. On the other hand, as the crystal is offset to positive angles, the negative cascaded nonlinearity compensates the material nonlinearity and together with positive cavity group delay dispersion leads to the gaussian output spectrum and soliton-like pulse. This effect is investigated further in time domain in our recent paper [20].

Unstable zone II. Since the investigated resonator has two instability zones, we also measured the output beam dependence on the phase matching angle with the curved mirror distance fixed at $\Delta L = -0.6$ mm (close to unstable zone II). The measured sagittal and tangential beam radii are shown in Fig. 5(A) at different values of the phase matching angle. The green points correspond to the measured beam profile (Fig. 5(B)), simulated beam profile (Fig. 5(C)) and measured spectra (Fig. 5(D)) at these exact angle offsets. The observed change in the radii indicates that the positive crystal offsets leads to negative (defocusing) cascaded nonlinearity which shifts the stability towards configuration supporting highly elliptical mode in sagittal (Y) direction. The red area indicates the unstable angle offset region, when the resonator is "pushed" towards the unstable part of zone II shown in Fig. 2(A). The simulated beam profiles closely resemble the experimental ones even though the entire numerically simulated region is shifted to smaller crystal offset angles. This can be explained by noting that the simulated output power is higher than experimentally measured, and therefore the impact of simulated cascaded nonlinearity is stronger. The positive crystal offsets lead to highly elliptic beams and TEM01 like structures. This can be explained by the smaller beam radius at the crystal in zone II compared to zone I: tighter beam produces higher
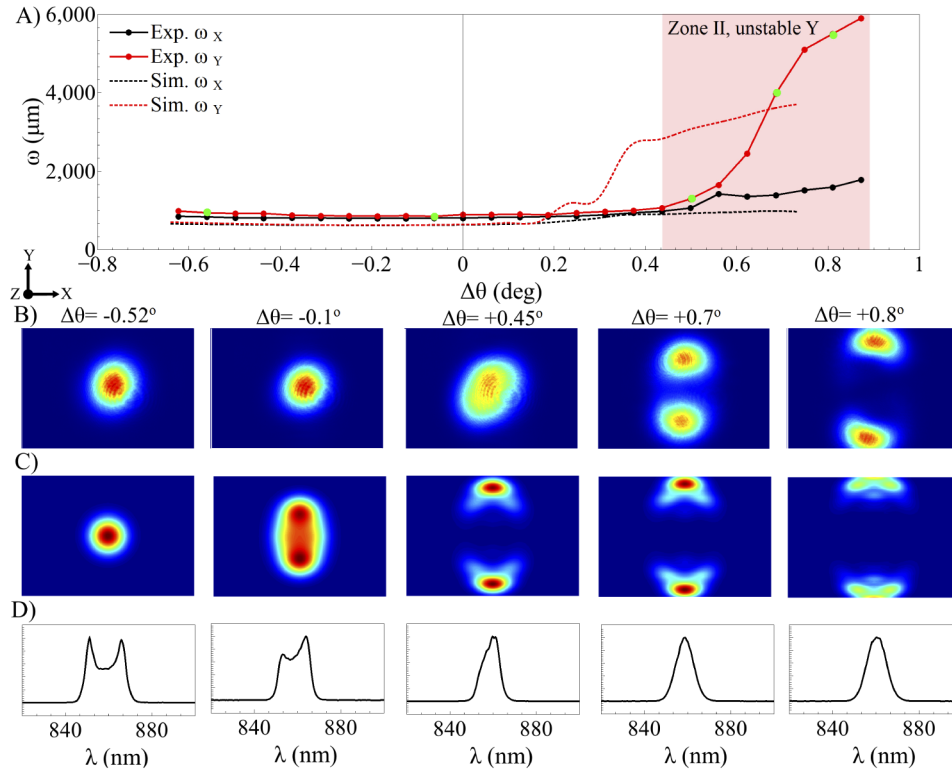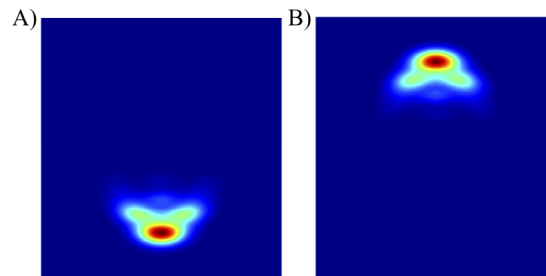
Fig. 4. A) The experimentally measured and numerically simulated second-moment radii (2σ) dependence on the nonlinear crystal angle detuning when resonator is aligned in zone I. The radii are calculated separately for tangential (X) and sagittal (Y) planes. Blue points indicate the crystal angles where experimental, numerically simulated beam profiles and output spectra are shown below. B) Experimentally measured beam profiles corresponding to different values of $\Delta\theta$. C) Numerically simulated output beam profiles corresponding to different values of $\Delta\theta$. D) Experimentally measured pulse spectra corresponding to different values of $\Delta\theta$. The central wavelength is fixed at 860 nm. The red color area indicates the experimentally observed unstable or highly asymmetric tangential (X) plane region in zone I.

intensity and the defocusing nonlinearity turns into stronger nonlinear lens. Further investigation of the TEM01-like structure shows that this is not a stable mode, but an unstable beam which replicates itself every second pass as shown in Fig. 6. This clearly indicates that the nonlinear lens is strong enough to „push" the resonator out of the stability. Essentially each of the sub-beams in the double beam pattern runs at half of fundamental repetition rate with a constant one period offset. The measured spectra in Fig. 5(D) indicate even stronger SPM contribution to spectral broadening when compared to zone I, as the overall nonlinearity is higher.

To quantify the cascaded nonlinearity induced nonlinear focusing / defocusing, further simulations were carried out. The nonlinear phase was extracted from numerical model (Eqs. (1) to (3)). A single pass through the OPO crystal with varying crystal angles was simulated with experimentally observed steady state OPO parameters at the center of the tuning curve: fixed pulse duration τ =180 fs, fixed intracavity average power P = 8 W, signal wavelength of 860 nm. The on-axis nonlinear phase was fit with a parabola and from the curvature the nonlinear focal length was calculated. The results are shown in Fig. 7(A) with separate calculation for zone I and zone II. The blue and green calculation points are of the nonlinear focal length values which

Fig. 5. A) The experimentally measured and numerically simulated second-moment radii (2σ) dependence on the nonlinear crystal angle detuning when resonator is aligned in zone II. The radii are calculated separately for tangential (X) and sagittal (Y) planes. Blue points indicate the crystal angles where experimental, numerically simulated beam profiles and output spectra are shown below. B) Experimentally measured beam profiles corresponding to different values of Δθ. C) Numerically simulated output beam profiles corresponding to different values of Δθ. D) Experimentally measured pulse spectra corresponding to different values of Δθ. In all panels signal central wavelength is fixed at 860 nm. The red color area indicates the experimentally observed unstable or highly asymmetric sagittal (Y) plane region in zone II.

Fig. 6. A) The numerically simulated steady state N_{th} pass output beam profile when resonator is operated in zone II. B) The numerically simulated steady state $N_{th}+1$ pass output beam profile when resonator is operated in zone II. For both panels the crystal detuning angle is Δθ=+0.45° and the signal central wavelength is fixed at 860 nm. Steady state defines pass to pass stable output power.

correspond to the experimentally and numerically simulated beam profiles / spectra shown in the previous figures. The zero of nonlinear phase corresponds to an infinite radius of the curvature of the nonlinear lens, implying that positive material nonlinearity is compensated by negative cascaded nonlinearity.
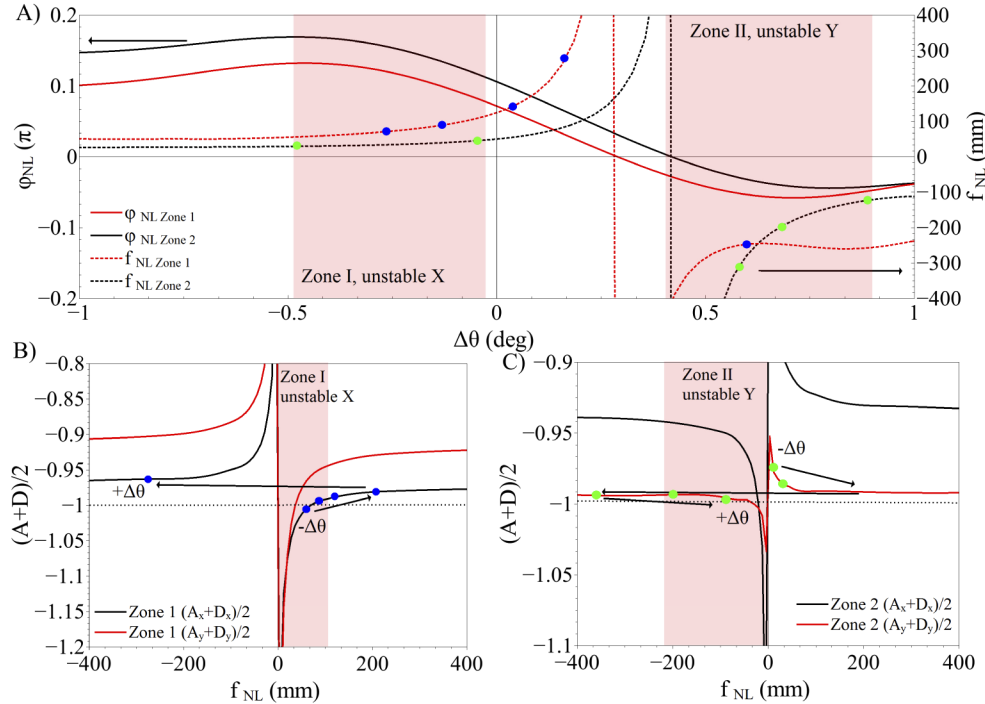
Fig. 7. A) The calculated peak nonlinear phase and nonlinear focal length dependence on the nonlinear crystal angle detuning when resonator is aligned in zone I and zone II. B) The calculated tangential (X) and sagittal (Y) resonator stability parameter $(A + D)/2$ dependence on nonlinear lens focal length when resonator is aligned in zone I. C) The calculated tangential (X) and sagittal (Y) resonator stability parameter $(A + D)/2$ dependence on nonlinear lens focal length when resonator is aligned in zone II. In all panels signal central wavelength is fixed at 860 nm, the red color areas indicate the experimentally observed unstable or highly asymmetric regions in zone I and zone II. In all panels blue and green points indicate the experimental and simulated beam profiles, spectra measurements shown in Fig. 4 and Fig. 5.

Figure 7(B) and Fig. 7(C) shows ABCD matrix stability parameter dependence on nonlinear focal length for both zone I and zone II. The nonlinear lens value from Fig. 7(A) is used as ABCD matrix lens seen by forward propagating beam when optical parametric amplification takes place. The backward propagating beam sees only a fixed positive lens induced by the material nonlinearity. The blue and green points with arrows indicate the shift of nonlinear focal length and corresponding stability while crystal is detuned from negative to positive angles. Blue zone I points are plotted for the unstable X tangential plane and green zone II points are plotted for the unstable Y sagittal plane. The red areas indicate the unstable region when resonator is "pushed" towards the unstable zone I or zone II as shown in a linear stability plot of Fig. 2(A). The stability maps explain the experimental results – in zone I, the initial negative crystal offsets ($\Delta\theta \sim -0.25^o$) and mildly focusing cascaded nonlinearity ($f_{NL} = +125$ mm) lead to unstable resonator at tangential X plane. When the crystal is positively offset ($\Delta\theta \sim 0.4^o$), nonlinear focal length becomes infinite and with further crystal angle increase ($\Delta\theta \sim 0.65^o$) the resonator is

stabilized with weakly defocusing cascaded nonlinearity ($f_{NL} = -250$ mm). In zone II, the initial negative crystal offsets ($\Delta\theta \sim -0.5^o$) and strongly focusing cascaded nonlinearity ($f_{NL} = +30$ mm) lead to stable resonator at sagittal Y plane. When the crystal is positively offset ($\Delta\theta \sim 0.25^o$), nonlinear focal length becomes infinite and with further increase in crystal angle ($\Delta\theta \sim 0.9^o$) the resonator becomes unstable with mildly defocusing cascaded nonlinearity ($f_{NL} = -110$ mm).

　　We have also performed a test to see if the asymmetry of the beam is not induced by resonator misalignment due to the rotation of the crystal. To test this, we tuned the central wavelength away from the exact phase matching by changing the cavity length (i.e. synchronous pumping condition) at fixed crystal angle. This way, we could induce the equivalent phase mismatch as by rotating the crystal, but in this case the resonator geometry is left intact [16]. In zone I, the wavelength was tuned to 820 nm, in zone II to 900 nm with the crystal angle optimized for 860 nm. The same asymmetric beam patterns were generated, indicating that the process is purely cascaded nonlinearity induced nonlinear focusing / defocusing.

　　Furthermore, it is instructive to quantify the QCN induced nonlinear lens wavelength dependency. Based on the simulations presented in our paper [21], the nonlinear phase dependence on wavelength was extracted for the LBO adjusted for optimal conversion efficiency at 860 nm. Relative to 860 nm, there is a $-0.05\ \pi$ nonlinear phase shift at 820 nm and a $0.1\ \pi$ nonlinear phase shift at 900 nm. The phase relationship is quasi linear in wavelength range of 820 nm to 900 nm. Therefore, in the spatial domain 820 nm is self-defocused, while 900 nm is self-focused and this acts as a longitudinal chromatic aberration. These phase mismatched wavelengths of 820 nm and 900 nm correspond to the equivalent phase mismatch induced to 860 nm by the angle offsets $\Delta\theta \sim -0.5^o$ and $\Delta\theta \sim 0.9^o$ shown in the Fig. 7(A). The same nonlinear focal lengths could be attributed to the phase mismatched wavelengths: λ=820 nm would focus with $f \sim 30$ mm ($D \sim 33$ m^{-1} at $\Delta\theta \sim -0.5^o$) and λ=900 nm would focus with $f \sim -110$ mm ($D \sim -9$ m^{-1} at $\Delta\theta \sim 0.9^o$). Therefore, the chromatic aberration would be extremely strong for a spectrum bandwidth of $\Delta\lambda = 80$ nm (14 fs pulse duration pulses), this bandwidth is supported by an amplification bandwidth of a crystal if resonator's group delay dispersion is minimized [21]. Therefore, the QCN induced spatial domain longitudinal chromatic aberration should be an effect limiting the beam quality of generated short pulses not only in femtosecond OPO, but also in travelling wave parametric amplifiers operated under phase mismatch.

　　On the other hand, the pulse bandwidth generated in our setup was much narrower with $\Delta\lambda = 6$ nm. The nonlinear phase difference between the side wavelength components is $\Delta\varphi = 0.015\ \pi$, leading to the nonlinear focal lengths of $f \sim 39$ mm ($D \sim 25.5$ m^{-1}) at 857 nm and $f \sim 35$ mm ($D \sim 28.5$ m^{-1}) at 863 nm. There is 3 m^{-1} diopters focusing difference across the spectrum bandwidth, which is collimated by the spherical mirrors, so the effect is not evident at the output, nevertheless, it could be pronounced for a broader spectrum. These considerations also hint that full spatial and time domain simulation of the phase mismatched optical parametric oscillators or amplifiers should show the interplay between aforementioned effects, which could lead to such a peculiar effect as simultaneous generation of stable and unstable resonator modes having different wavelengths. Further study is needed to confirm this hypothesis.

　　It is important to show that the observed effects are not influenced by critical self-focusing. With the measured pulse duration of the OPO $\tau = 180$ fs, the calculated peak power is 400 kW at $\Delta\theta \sim -0.5^o$. Calculation of the maximum nonlinear refractive index from the nonlinear phase at the $\Delta\theta \sim -0.5^o$ leads to $n_2 \sim 10 \times 10^{-20}$ m^2/W. The calculated critical power $P_{crit} = 0.148\ \lambda^2/n\,n_2$ results in ~ 700 kW. The critical power is defined as the peak power at which the diffraction is balanced by self-focusing. Therefore, our experimental conditions are below the critical self-focusing and the observed mode formation patterns should be influenced only be the cascaded nonlinearity induced stability change and not by mode self-diffraction or filament formation.

　　Generally, the nonlinear distortions of the spatial laser mode are regarded as harmful and avoided in the design of laser process. However, the success of the now ubiquitous Kerr lens

modelocking shows that they could also be applied productively. If the double beam pattern observed in zone II Fig. 5 could be made controllable and stable enough, it could lead to some interesting applications. For instance, in Stimulated Raman Microscopy using only one beam which has repetition rate $f/2$ as a tunable wavelength laser source together with part of fundamental oscillator output with repetitition rate f. The tunable beam could be demodulated with lock-in amplifier at $f/2$ without an additional fast modulator at $f/2$. Another application would be having one of these beams polarization rotated by 90° and recombining them extracavity. This would lead to a tunable wavelength source where every second pulse is with orthogonal polarization. Such a laser source could be used for polarization sensitive nonlinear imaging techniques where difference between the signals from each of the pulse in a pair could be used for background subtraction. Naturally, to enable such applications, nonlinear spatial phenomena occurring in OPO cavities would have to be investigated in much greater detail, finding the ways of their stable generation, control and investigating their applications.

To conclude, design guidelines for high power femtosecond oscillators should be drawn. For example, let us consider the same Z-fold OPO resonator as investigated in this paper. With low pump power and neglible nonlinear lens, resonator could be aligned at the middle of one of the stability zones with the tangential stability of $(A + D)/2 = -0.5$. As shown in section 3, direct insertion of the experimental parameters to the Eq. (4) leads to the nonlinear focusing power of $D \sim 24$ m^{-1} under the exact phase matching and this value slightly changes the stability of the resonator. The extreme nonlinear lens focusing power of $D \sim 120$ m^{-1} would drive the tangential stability to a value of $(A + D)/2 = -1$, leading to an unstable resonator. Simple scaling calculation of Eq. (4) shows that this extreme nonlinear lens power value could be reached by 5-fold larger intracavity signal power (~ 4 W of the output signal power) or effective nonlinearity ($n_2 \sim 15 \times 10^{-20}$ m^2/W), or 1.5-fold smaller waist size (~ 33 μm waist size at the crystal) or a combination of all these parameters. The critical self-focusing would as well impact the resonator mode properties and a further study is needed to investigate and decouple the influence of both the linear stability shift and critical self-focusing with increasing intensity or nonlinearity. Therefore, in order to scale the output power and prevent the aforementioned effects, the OPO should be operated with negligible phase mismatch and correspondingly larger mode size at the nonlinear crystal.

5.   Conclusions

It was shown that the cascaded nonlinearity induced self-focusing and defocusing are strong enough to change resonator's stability. The mode properties are impacted if operating near the resonator's stability edge. With tuning of a phase mismatch, the calculated parabolic part of the cascaded nonlinearity lens focal length changes from $f \sim 30$ mm ($D \sim 33$ m^{-1}) to infinity and back to $f \sim -110$ mm ($D \sim -9$ m^{-1}). Such high lens powers, operation near stability range and resonator astigmatism promoted generation of axially asymmetric or pass-to-pass unstable resonator modes. It was shown that phase mismatched optical parametric oscillation changes the physical operation of resonator from linear to ring-like with two nonlinear crystals having two different focusing powers. A numerical simulation in XYZ spatial domain and a calculation with ABCD matrix approach confirmed the experimental results and allowed interpreting the investigated peculiarities. Calculations showed that the QCN induced spatial nonlinear phase should lead to severe longitudinal chromatic aberrations for broad spectrum pulses. Operating the cascaded nonlinearity crystal intra-cavity near the stability limit allowed probing weak nonlinear effects which would be hard to investigate in a single pass extra-cavity setup.

Funding

Acknowledgement

Disclosures

I. Stasevičius, M. Vengris (part-time) are paid employees of "Light Conversion", Vilnius, Lithuania.

References

1. D. T. Reid, J. M. Dudley, M. Ebrahimzadeh, and W. Sibbett, "Soliton formation in a femtosecond optical parametric oscillator," Opt. Lett. **19**(11), 825–827 (1994).
2. M. Ghotbi, A. Esteban-Martin, and M. Ebrahim-Zadeh, "BiB_3O_6 femtosecond optical parametric oscillator," Opt. Lett. **31**(21), 3128–3130 (2006).
3. M. Jankowski, A. Marandi, C. R. Phillips, R. Hamerly, K. A. Ingold, R. L. Byer, and M. M. Fejer, "Temporal simultons in optical parametric oscillators," Phys. Rev. Lett. **120**(5), 053904 (2018).
4. X. Zhang and H. Giessen, "Four-wave mixing based on cascaded second-order nonlinear processes in a femtosecond optical parametric oscillator operating near degeneracy," Appl. Phys. B **79**(4), 441–447 (2004).
5. T. Gottschalll, J. Limpert, and A. Tunnermann, "Ultra-short pulse fiber optical parametric oscillator," Opt. Lett. **42**(17), 3423–3426 (2017).
6. G. M. Gale, M. Cavallari, and F. Hache, "Femtosecond visible optical parametric oscillator," J. Opt. Soc. Am. B **15**(2), 702–714 (1998).
7. G. I. Stegeman and D. J. Hagan, "χ^2 cascading phenomena and their applications to all-optical signal processing, mode-locking, pulse compression and solitons," Opt. Quantum Electron. **28**(12), 1691–1740 (1996).
8. T. Lang, A. Harth, J. Matyschok, T. Binhammer, M. Schultze, and U. Morgner, "Impact of temporal, spatial and cascaded effects of pulse formation in ultra-broadband parametric amplifiers," Opt. Express **21**(1), 949 (2013).
9. G. Arisholm, R. Paschotta, and T. Sudmeyer, "Limits of the power scalability of high-gain optical parametric amplifiers," J. Opt. Soc. Am. B **21**(3), 578–589 (2004).
10. G. Cerullo, S. De Silvestri, V. Magni, and L. Pallaro, "Resonators for Kerr-lens mode-locked femtosecond Ti:sapphire lasers," Opt. Lett. **19**(11), 807–809 (1994).
11. A. Penzkofer, M. Wittmann, M. Lorenz, E. Siegert, and S. Macnamara, "Kerr lens effects in a folded-cavity four-mirror linear resonator," Opt. Quantum Electron. **28**(4), 423–442 (1996).
12. R. Šuminas, G. Tamošauskas, G. Valiulis, and A. Dubietis, "Spatiotemporal light bullets and supercontinuum generation in β-BBO crystal with competing quadratic and cubic nonlinearities," Opt. Lett. **41**(9), 2097–2100 (2016).
13. R. Šuminas, G. Tamošauskas, V. Jukna, A. Couairon, and A. Dubietis, "Second-order cascading-assisted filamentation and controllable supercontinuum generation in birefringent crystals," Opt. Express **25**(6), 6746–6756 (2017).
14. M. Seidel, J. Brons, G. Arisholm, K. Fritsch, V. Pervak, and O. Pronin, "Efficient High-Power Ultrashort Pulse compression in Self-Defocusing Bulk Media," Sci. Rep. **7**(1), 1410 (2017).
15. F. Hache, A. Zeboulon, G. Gallot, and G. M. Gale, "Cascaded second-order effects in the femtosecond regime in β-barium borate: self-compression in a visible femtosecond optical parametric oscillator," Opt. Lett. **20**(14), 1556–1558 (1995).
16. I. Stasevicius, G. Martynaitis, and M. Vengris, "Cascaded nonlinearities in high-power femtosecond optical parametric oscillator," J. Opt. Soc. Am. B **37**(3), 721–729 (2020).
17. R. Laenen, H. Graener, and A. Laubereau, "Evidence for chirp reversal and self-compression in a femtosecond optical parametric oscillator," J. Opt. Soc. Am. B **8**(5), 1085–1088 (1991).
18. R. DeSalvo, D. J. Hagan, M. Sheik-Bahae, G. Stegeman, and W. E. Van Stryland, "Self-focusing and self-defocusing by cascaded second-order effects in KTP," Opt. Lett. **17**(1), 28–30 (1992).
19. C. Conti, S. Trillo, G. Gallot, G. M. Gale, P. Di Trapani, J. Kilius, A. Bramati, S. Minardi, W. Chinaglia, and G. Valiulis, "Effective lensing effects in parametric frequency conversion," J. Opt. Soc. Am. B **19**(4), 852–859 (2002).
20. I. Stasevicius and M. Vengris, "Exploiting optical nonlinearities for group delay dispersion compensation in femtosecond optical parametric oscillator," Opt. Express **28**(18), 26122–26136 (2020).
21. I. Stasevicius and M. Vengris, "Controlled soliton formation in a femtosecond optical parametric oscillator with positive group delay dispersion," J. Opt. Soc. Am. B **37**(10), 2956–2967 (2020).
22. G. P. Agrawal, *Nonlinear Fiber Optics* 5th Edition, Academic Press, (2013).
23. D. Nikogosyan, *Nonlinear Optical Crystals: A Complete Survey*, Springer, (2015).
24. N. Hodgson and H. Weber, *Laser Resonators and Beam Propagation*, Springer, (2005).
25. R. Hamerly, A. Marandi, M. Jankowski, M. M. Fejer, Y. Yamamoto, and H. Mabuchi, "Reduced models and design principles for half-harmonic generation in synchronously-pumped optical parametric oscillators," Phys. Rev. A **94**(6), 063809 (2016).
26. A. E. Siegman, *Lasers*, University Science Books, (1986).